Characterisation of hydrogen jet flames under different pressures with varying coflow oxygen concentrations

Jordan A.C. Kildare [a,*], Michael J. Evans [b], Douglas B. Proud [a], Rey Chin [a], Zhao Tian [a], Paul R. Medwell [a]

[a] School of Electrical and Mechanical Engineering, The University of Adelaide, Adelaide, 5005, Australia
[b] UniSA STEM, The University of South Australia, Mawson Lakes, 5095, Australia

ARTICLE INFO

ABSTRACT

The elevated temperature of hydrogen combustion increases the formation of thermal NO_x. Moderate or intense low oxygen dilution (MILD) combustion is known to reduce NO_x emissions and increase thermal efficiency. Pressure is often also used for increasing thermal efficiency. The impact that pressure has on fluid dynamics and chemical kinetics is especially relevant in MILD combustion conditions. Hydrogen jet flames issuing into a hot and vitiated coflow were imaged using OH^* chemiluminescence at different pressures (1–7 bar) and oxygen levels (3–9% by vol.). Laminar flame simulations complemented the experiments. The observed mean radial OH^* width increased with increased pressure, but only at O_2 content less than 9%, suggesting that pressure has greater influence on kinetics when oxygen is reduced. The integrated OH^* signal strength remained constant at 3% coflow O_2, despite an apparent increase in flame width, suggesting a spatial broadening of the flame with pressure. Numerical results indicate that at 3–6% O_2, conditions for MILD combustion of H_2 are met across a wide range of strains and pressures, supporting the experimental observations for 3% O_2.

Introduction

Combustion of carbon-free fuels, such as hydrogen, has become more of a focus as society shifts away from fossil fuels. Hydrogen is noted for its high specific energy, as well as zero carbon products. These characteristics make hydrogen ideal for use where electrification is not a viable alternative, instead taking advantage of advanced combustion concepts. However, at the elevated temperatures achieved from burning hydrogen with air, thermal NO_x becomes more prevalent [1].

Throughout the transition from fossil fuels, advanced combustion concepts are being employed to help reduce emissions from existing fuels, and to increase thermal efficiency. Moderate or intense low-oxygen-dilution (MILD) combustion is one such concept. Reductions in NO_x and peak temperatures were observed in previous studies of MILD combustion, showing promise when combined with fuels such as hydrogen [2–5]. Similarly, recent findings have indicated that reduced oxygen and elevated pressure reduce NO_x formation in CO/H_2 laminar flames [6]. Combining MILD combustion with hydrogen fuel shows

promise for reducing the thermal NO_x production of hydrogen-air combustion.

There are several definitions of MILD combustion, such as (i) well-stirred reactor (WSR) temperature rise [7]; (ii) no net negative heat release rate [8,9]; (iii) and monotonic S-shaped curve [10]. The conditions required for MILD combustion are generally achieved through lean combustion of fuel upstream of the test section, or through exhaust gas recirculation (EGR) [11–13]. The result of these conditions is a distributed reaction zone, with elevated average temperature, but reduced peak temperatures [14]. Given that thermal NO_x formation (from high temperature combustion processes) is heavily temperature dependent, reduced peak temperatures reduce NO_x production [1,2,15,16].

Chemical effects of low oxygen combustion can be analysed using a jet in hot coflow (JHC) burner configuration. The JHC configuration decouples the chemical kinetics from the fluid flow, emulating the conditions of EGR without the complex flow patterns, to enable advancement of fundamental-level understanding. H_2/CH_4 (1:1 by vol.) jet flames in a JHC burner have been studied, finding that with 3% O_2 in the coflow, the peak temperature, OH concentration, and NO concentration were significantly reduced compared with 9% O_2 [2]. Subsequently, concentrations of O, H, OH, and OH^* have been used to determine heat release computationally for H_2/CH_4 jets in the JHC configuration [17]. It was found that the optimal method of heat release rate determination was dependent on both operating conditions and fuel chemistry, indicating a lack of universal method for different flame types [17].

Addition of hydrogen into methane jets in a JHC configuration was found to increase the stability, and decrease lift-off height [18]. Apparent lift-off height also tends to reduce with an increase in O_2 from 3% to 9% by volume in a JHC configuration, using n-heptane as fuel [9]. This is in contrast to observations using ethanol, methane, and ethylene as the fuel in the same apparatus, where non-monotonic variation in lift-off height with coflow O_2 concentration was noted [9,12]. Similar observations have been made using diluted acetylene jet in a JHC configuration, whereby a decrease in O_2 of the coflow resulted in a transition from an attached to a lifted flame [9,19]. The separate observations imply increasing hydrocarbon chain length results in a reversal of lift-off height behaviour [9,19].

Lift-off height was found to be affected by the external confinement of the flame for a methane jet in vitiated coflow, with an increase in the downstream confinement resulting in reduced lift-off height [20]. Hydrogen jet flames in Ar, N_2, and CO_2 diluted hot coflows have shown dependence on diluent species and coflow temperature for lift-off height characteristics [21]. Addition of hydrogen into a parallel methane jet combustor at 15% O_2 was found to decrease stability overall, after first reducing the lift-off height of the flame [22].

A vitiated coflow burner (VCB) using H_2 diluted with N_2 in the jet was used to identify that autoignition contributes towards the stabilisation of lifted H_2 flames in hot and vitiated coflows [23]. Modelling of H_2/CH_4 JHC flames in MILD conditions has shown that heat release increases significantly with an increase in O_2, and that addition of hydrogen tends to reduce the reaction zone volume, and the radial spread of the flame [24]. There is also a greater sensitivity of the turbulence

decay and flame entrainment to oxygen level when the hydrogen content is increased [24]. Addition of hydrogen to a methane EGR burner was found to result in reduced ignition delay and greater reactivity [25]. Increasing oxidiser velocity in this configuration supported the transition to MILD combustion [25]. Comparisons of dimethyl ether (DME) and ethanol flames at varying low oxygen conditions have shown that the H_2/O_2 oxidation pathways play important roles in the oxidation of both fuels, despite their different decomposition pathways [26]. However, whilst a significant amount of research has focussed on low oxygen, elevated temperature combustion, less has been focussed on pressurised combustion in these conditions.

An increase in fluid pressure before a combustion process typically results in an increase in thermal efficiency [27–29]. Compression stages in a gas turbine utilise this concept before the combustion stage to increase efficiency. This is effective in contemporary engines as the chemical and fluid timescales are significantly different, and oxygen content is significantly higher, minimising the chance of reaction quenching [30]. However, in MILD combustion, oxygen content is low, and the fluid and chemical timescales are very similar, indicated by a Damköhler number of unity [31–33]. Hence, increasing pressure has a marked influence on the combustion processes from both a fluidic and a chemical kinetics perspective [32,33].

Pressure plays a considerable role on both the fluid dynamics and the chemical kinetics of a combusting flow, as well as the coupling between these two components. An increase in pressure increases density, affecting the turbulence field and increasing the number density of reactants. Subsequently, mixing characteristics and reaction rates are directly affected [34,35]. Increasing pressure also changes the fluid timescale, as flow speed reduces, allowing for longer residence times and hence more complete reactions [36]. Changes in pressure directly impact on the reaction rate constants through the activation volume property, and contribute towards changes in preferential reaction pathways [37–39]. The result is a complex influence of pressure on combustion, which is particularly prevalent where fluid and chemical timescales are of a similar order, such as in MILD combustion [7]. Hence, to effectively implement MILD combustion in pressurised conditions, these flames require in depth investigation.

A FLOX® burner oriented horizontally using CH_4 and heated air at 8 bar demonstrated an asymmetric OH distribution in the vertical plane, with flame stabilisation driven by intense recirculation [40,41]. Hydrogen jet flames at 12 bar have been studied, finding that differential diffusion is particularly important in accurately modelling these flames [42]. The effect of molecular diffusion in CH_4-H_2 flames was found to be extremely important in other work, due to the presence of H_2 [43–46]. Differential diffusion has also been indicated to be especially important in other dual-fuel hydrogen combustion modelling [47]. A H_2/CH_4 jet in preheated crossflow at elevated pressures (10 bar and 15 bar) has shown minimal impact on the mean distribution of OH^* signal and flame structure with a change in pressure [48]. The conditions were not low oxygen, and hence do not have the same balance between chemical and fluid timescales that pressure will have a marked effect on. Recent work investigating high

injection pressure, elevated temperature, confined hydrogen jet combustion has indicated that reduction in ambient O_2 increases lift-off height, whilst an increase in ambient temperature results in earlier onset of autoignition [49]. Despite large bodies of work dedicated to hydrogen combustion at pressure, there has been minimal investigation of hydrogen jet flames and the effect pressure has on combustion in low oxygen, high temperature conditions.

As discussed, characterisation of turbulent hydrogen flames in both elevated pressure and low oxygen conditions is limited, despite work focussed on the two components separately. To address this gap, OH^* chemiluminescence has been imaged in a pressurised JHC configuration, at various pressure and oxygen conditions. The experimental observations are accompanied by opposed-flow laminar flame calculations across a significant range of conditions, to gain better insight into the characteristics of these flames.

Method

Experimental setup

Images of OH^* chemiluminescence were taken from turbulent hydrogen jet flames within a confined and pressurised JHC (CP-JHC) burner. The CP-JHC allows independent control of coflow temperature, O_2 concentration, and bulk flow velocities [50]. The central fuel jet has a 4.6 mm inner diameter, with hydrogen as the fuel. The temperature of the fuel at the exit of the jet is < 350 K. The coflow surrounds the jet, and has an inner diameter of 100 mm. The coflow consists of lean combustion products from H_2/CH_4 (1:1 by vol.), and air. The products are assumed to be in equilibrium, noting the long distance and residence time between the burner used to generate the coflow and the exit plane of the central fuel jet. Equilibrium calculations were used to determine the composition of the major species at the given pressures and experimental temperatures for use in the chemical kinetics simulations, with the species mole fractions presented in Table 1. The use of H_2/CH_4 rather than pure H2 for the coflow fuel is for consistency with other JHC experiments [2,9,10,26], and with other experiments performed with the same CP-JHC apparatus [50]. As such, the composition was kept consistent for comparability. The air flow rate is varied to achieve desired O_2 content of 3%, 6%, and 9% by volume whilst maintaining a constant heat input into the flow. While this does affect the jet-coflow momentum ratio, the bulk velocity of the coflow is two orders of magnitude smaller than that of the jet, making this impact relatively negligible. Pressure in these experiments is increased to a maximum of 7 bar, at coflow temperatures of 1100 K (refer Section Experimental Conditions).

OH^* chemiluminescence was imaged through a quartz window perpendicular to the flow. A diagram of the experimental setup can be found in the Supplementary Material Section 1. OH^* is the electronically excited OH radical, releasing a photon during the de-excitation process. OH^* is a strong indicator of reaction zones in combustion, as primary production pathways are through the combination of the combustion intermediates, atomic H and O, and CH with O_2 [51]. OH^* releases light primarily with a central emission wavelength of ~308 nm resulting from the transition from state $A^2\Sigma^+$ to $X^2\Pi$ [52]. This was imaged using an intensified charge coupled device (ICCD) camera, fitted with an optical bandpass filter centred at 310 nm, with a bandwidth of 10 nm. The images analysed have been time-averaged over a 10 s period. OH^* chemiluminescence is a qualitative diagnostic and so will primarily be used to analyse trends rather than present quantitative data for direct model validation or theory development. As this study involves the initial characterisation of H_2 jet flames in MILD and pressurised conditions, OH^* chemiluminescence is the primary diagnostic being presented here, with supporting analysis using the laminar opposed-flow diffusion flame simulations for chemical kinetic analysis, discussed in Section Chemical Simulations.

Experimental conditions

Table 2 shows the experimental cases undertaken in this work. The stoichiometric mixture fraction (Z_{st}) reported in Table 2 is calculated based on the fuel (H_2) and oxidiser composition for each coflow condition (presented in Table 1). The jet consisted of hydrogen ($\gtrsim$ 99.5%), at a constant mass flow rate across all cases. The jet mass flow rate corresponded to a bulk mean Reynolds number of approximately 10,000 for all pressures, in order to maintain similar turbulence characteristics. Three pressures were investigated: 1 bar, 5 bar, and 7 bar absolute. The coflow O_2 contents were 3%, 6% and 9% by volume. The coflow was kept within a range of 1010 K–1100 K across the cases. The naming convention in Table 2 refers to the fuel type (e.g. "H" for hydrogen), coflow O_2 content by mole (e.g. "3" for 3% O_2), and operating pressure (e.g. "P1" for 1 bar), resulting in a name of H3–P1 for this example case.

The pressure was held within ±0.01 bar. Fuel and coflow flow rates are controlled via digital mass flow controllers (MFCs), with errors of ±0.5% of the reading. Temperature of the coflow is monitored with an R-type thermocouple.

Data processing

Chemiluminescence imaging results in a line-of-sight integrated image. Line-of-sight images are useful for understanding the typical flame appearance, however, the underlying flame structure is not readily determined without transforming the original image. In the case of a JHC type burner, the flame is axisymmetric about the jet centre, and so an inverse Abel transformation can be conducted to better visualise the reaction zone of the flame. The inverse Abel transform, applied in this work, is where a line-of-sight integrated image is converted into the equivalent three-dimensional object, or the 2D cross-section of that three-

Table 1 – Mole fractions of major species for each coflow composition.				
Oxygen content	O_2	N_2	H_2O	CO_2
3%	0.03	0.72	0.19	0.06
6%	0.06	0.73	0.16	0.05
9%	0.09	0.74	0.13	0.04

Table 2 – Experimental cases analysed. Bulk mean jet Reynolds numbers all approximately 10,000.						
Name	Pressure (bar)	Coflow O_2 (% vol)	Coflow Temp (K)	U_{coflow} (m/s)	U_{jet} (m/s)	Z_{st} (−)
H3–P1	1.0	3.0	1110	2.1	240	0.0044
H6–P1	1.0	6.0	1100	2.5	240	0.0088
H9–P1	1.0	9.0	1010	2.8	240	0.0131
H3–P5	5.0	3.0	1050	0.41	49	0.0044
H6–P5	5.0	6.0	1080	0.50	49	0.0088
H9–P5	5.0	9.0	1070	0.61	49	0.0131
H3–P7	7.0	3.0	1100	0.30	35	0.0044
H6–P7	7.0	6.0	1100	0.36	35	0.0088
H9–P7	7.0	9.0	1100	0.45	35	0.0131

dimensional object. A 2D cross-section view allows a clearer picture of the structure of the flame. As such, the experimental analysis presented in Section OH* Spread onward has been performed for the inverse Abel transformed data rather than the data presented in Section Typical Appearance. It should be noted that the general observations discussed in Section Typical Appearance are still applicable with the transformed images.

The Basis-Set Expansion Abel transform method was implemented in this case, building off of a Python implementation of this theory [53]. This method involves creating an analytically integratable basis set for a two dimensional image, based on the number of pixels along the radial axis. Linear algebra is then applied to perform the Abel, or inverse Abel transforms, depending on the desired direction. Dependence only on the image pixels makes this method agnostic to the actual radial profiles, making it highly versatile. As the resolution is maintained, sharp features of the image — ones that may otherwise be filtered out using different transformation methods — are generally still well preserved. The

result of applying this transformation is shown in Fig. 1, both as a two-dimensional comparison in Fig. 1(a), and as the change in radial profiles at several locations in Fig. 1(b). The radial profiles are normalised by the peak OH* intensity value five diameters downstream of the jet exit, for both the original and inverse cases, respectively.

Chemical simulations

The software CHEMKIN Pro was used to analyse flames in conditions similar to those presented in Table 2. A total of 7500 laminar opposed-flow diffusion flame calculations are performed, across a parametric study with the following three variables:

- Pressures from 1 bar to 13 bar (50 equi-spaced increments).
- O_2 concentration in the oxidiser from 3% to 9% (3 increments). Note that when the O_2 concentration is changed, the other oxidant stream concentrations change — refer Table 1.

(a) Line-of-sight (left) and inverse Abel (right) images

(b) Radial profiles
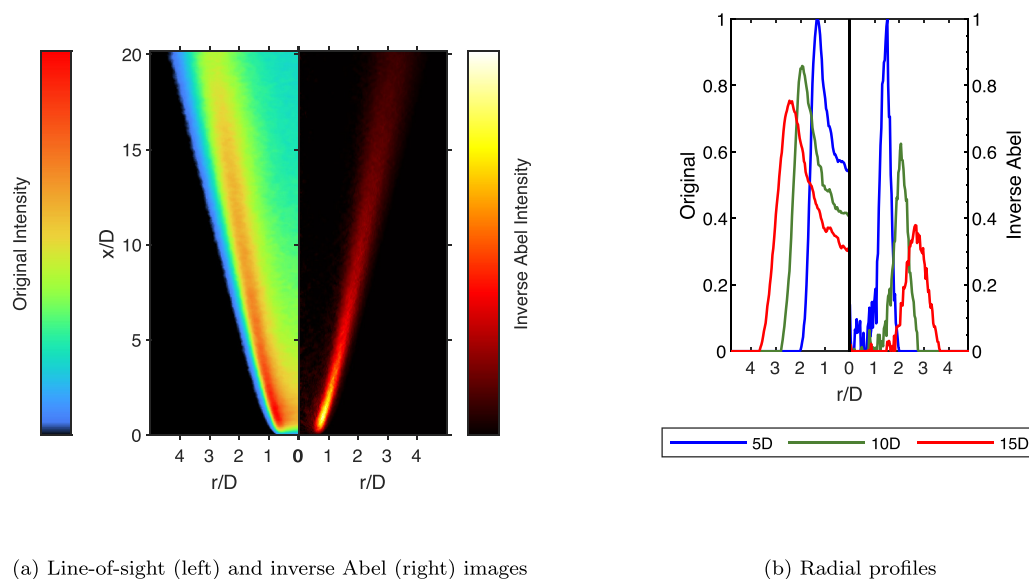
Fig. 1 – (a) Relative intensity of original image and inverse Abel transformed image demonstrating difference in OH* features. (b) Radial profiles at 5, 10, and 15 diameters downstream for original and inverse Abel transformed image, normalised by peak intensity. Data presented is for case H9–P7 (refer Table 2). Bottom border corresponds to the jet exit plane, with centreline at jet centre.

- Global strain rate from 1 s^{-1}–1000 s^{-1} (50 logarithmic increments).

The global strain rate was defined as $a = (U_{fuel} + U_{oxid})/L_D$, where L_D is the length of the domain. The OPPDIF routine in CHEMKIN was used to calculate the opposed flow laminar diffusion flames in these conditions. Velocities at each inlet were defined such that the momentum of each stream was equal, resulting in a stagnation plane approximately at the midpoint of the domain. When pressure is increased, density increases and hence, for identical velocities at different pressures, the mass flow rates will differ. In the experiments presented, the mass flow rates are constant with changes in pressure. In the simulations, the strain rate is varied by controlling the inlet velocities. For constant mass flowrate, as the pressure is increased the lower velocity will reduce strain rate. This is counteracted by increasing the velocity, and hence the mass flow rate. Hence, the strain rate and mass flowrate are coupled with pressure. When reporting the results as a function of strain rate (e.g. Figs. 11–13) lines of constant mass flowrate are also shown. The fuel stream is assumed to be entirely H$_2$, whereas the oxidant stream consists of equilibrium O$_2$, N$_2$, CO$_2$, H$_2$O, OH, NO, CO, O, and H at each operating condition. These equilibrium products result from the combustion of CH$_4$ and H$_2$ with excess air at 1050 K, approximately the midpoint of the measured experimental temperatures.

A modified version of the GRI-Mech 3.0 kinetic mechanism for methane combustion [54], including reactions for formation of both CH* and OH*, was implemented in the laminar flame calculations. The modification adds the species C$_2$, OH*, and CH*, as well as 26 elementary reactions, resulting in a mechanism of 56 species, and 351 reactions [51,55–57]. These modifications are made as OH* concentration is not necessarily coincident with OH concentration, which is a commonly used marker for combustion in laser diagnostic techniques [58,59]. As such, to accurately compare the trends of the chemiluminescence images with those of the flame calculations, incorporation of the excited form of this combustion radical is necessary. OH* has been found to coincide with locations of peak heat release in laminar flames in low oxygen combustion [58–60]. Heat release rate, dominant reactions, and temperatures can be extracted from laminar flame calculations to help explain observations from the experimental OH* chemiluminescence.

Two definitions of MILD combustion were investigated in relation to H$_2$ flames in low O$_2$ conditions using CHEMKIN. The Perfectly Stirred Reactor (PSR) definition states $(T_{final} - T_{initial}) < T_{ai}$, where $T_{initial} > T_{ai}$ [7]. The autoignition temperatures for the oxygen and pressure conditions analysed were determined from transient PSR simulations, also using CHEMKIN, rather than assuming a constant value across all conditions. The autoignition condition was defined as the temperature of the mixture at which an ignition delay of less than 0.5 s was observed, consistent with previous studies [61–64]. Determination of the ignition delay is performed by assessing whether there is a positive change in heat release at the maximum rate of change of temperature, i.e. the system is in thermal runaway [61,65,66]. The net negative Heat Release Rate (HRR) definition implies that MILD combustion can only occur where

there is no net negative heat release occurring [8,58]. The net heat release rate can be retrieved directly from the OPPDIF simulations.

Results and discussion

Experimental flames

Typical appearance

Fig. 2 presents line-of-sight images of OH* chemiluminescence from the nine combinations of pressure and coflow O$_2$ concentrations in this work (refer Table 2). The images are normalised against the maximum of case H9–P1. It is important to note that the images are time-averaged turbulent flames, and hence there is a significant contribution of turbulence to the appearance of the flame. Whilst an increase in pressure decreases the impact of small-scale eddies, the
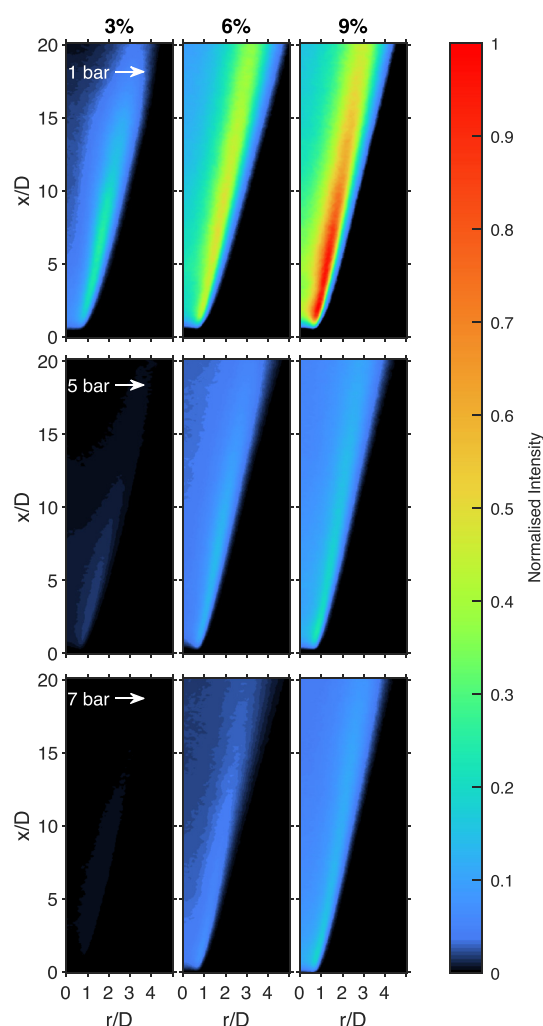

Fig. 2 — Comparison of line-of-sight OH* chemiluminescence intensity for all cases in Table 2, normalised to the peak value in the 9% 1 bar case. Images are 20D by 5D, with the bottom border edge corresponding to the jet exit plane.

larger scale eddies generated by the coflow impact on the overall flame shape, especially when time-averaged. Ideally, the coflow is considered as laminar, and so these effects are minimal, but they will still be present. Two initial trends can be observed in Fig. 2 in regards to peak OH^* intensity — reduction in OH^* with increased pressure, and a reduction in OH^* as O_2 is lowered. The latter trend is to be expected, as production of OH^* relies on the presence of O_2 in the coflow, however, the former observation requires a more in depth analysis from both a fluids and a chemical kinetics perspective. With an increase in pressure, diffusion of H_2 begins to play a more significant role in the flame structure, as turbulent transport reduces with the velocity, and residence time increases. The impact of H_2 diffusion is explored in more detail in Section OH^* Spread and Section H_2 Laminar Flame Characteristics. In Fig. 2, the uniformity of the chemiluminescence signal appears to increase in the flame zone when pressure is increased, with less noticeable peaks. This suggests a thickening of the flame, contributed to via higher diffusion of H_2, investigated further in Section Axial OH^* Profiles, and greater impact of large scale turbulent eddies. A thickening of reaction zone with a decrease in OH^* intensity is also suggestive of a broadening flame, discussed in Section H_2 Laminar Flame Characteristics and Section MILD Combustion in Laminar H_2 Flames.

Increases in coflow O_2 concentration also appear to affect the OH^* signal uniformity presented in Fig. 2. The core of the jet diminishes in OH^* intensity significantly when O_2 is reduced from 9% to 3%, especially in the 7 bar cases. This reduction in intensity suggests that pressure has a more significant influence on the chemical kinetics in extremely low O_2 conditions (3%), than it does at higher O_2 conditions (9%). Analysis of the chemical kinetics in these conditions is performed in Section Profiles in Mixture Fraction Space and Section Production of OH^* to better understand this behaviour. At 9% coflow O_2, an increase in the pressure shows a significant drop in OH^* intensity between 1 and 5 bar, but very little variation in intensity between 5 and 7 bar. However, more noticeable reductions in intensity are observed at 6% and 3% coflow O_2 concentrations when pressure is increased. These trends suggest an asymptotic reduction in OH^* intensity when O_2 content is increased, again indicating that pressure is more influential at very reduced coflow O_2. These trends are explored further using laminar flame calculations in Section Production of OH^*.

OH^* spread

OH^* production is at its peak at the stoichiometric mixture fraction (to be discussed in Section Profiles in Mixture Fraction Space), allowing visualisation of the spatial location of this mixture fraction. The peak of the time-averaged OH^* signals from the Abel-inverted line-of-sight images can be used to help differentiate the impact of pressure and coflow O_2 on the characteristics of the flame. Fig. 3 presents sample OH^* images for the 1 bar case at three O_2 levels, overlaid with the locations of peak OH^* at four heights and a linear fit through the data points. Plots of these lines for all experimental cases can be found in Figure SM2.1 of the Supplementary Material Section 2.
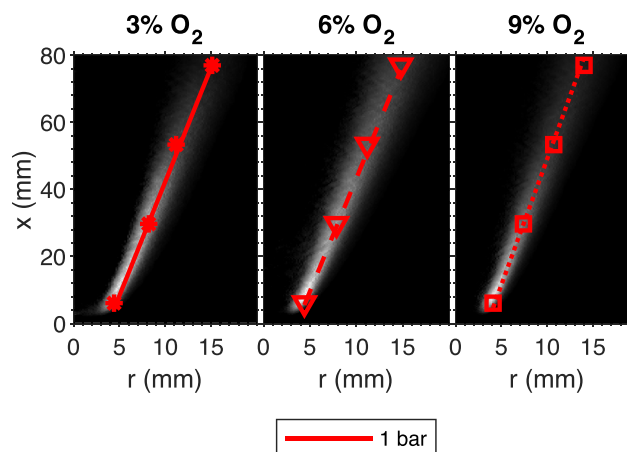

Fig. 3 – Lines of best fit for peak OH^* signal for 1 bar cases.

Key characteristics of the peak mean OH^* signal obtained from the data points in Fig. 3, such as the slope of the line, and the axis intercept, can be quantitatively compared through the spread angle, and the virtual origin, respectively. The virtual origin is an indicator of the self-similar zone of the jet, corresponding to a momentum point-source analogue of the jet, or in this case, the OH^* concentration point source [67]. The spread angle helps to differentiate the effect of pressure as compared to O_2 content on the OH^* concentration profile. In fixed coflow O_2 cases, if a change in pressure alters the spread angle, it indicates there is a change in the balance between the fluid and chemical timescales. OH^* virtual origin and spread angle are presented in Fig. 4.

At 3% coflow O_2, Fig. 4(a) shows that elevated pressure increases the spread angle of the peak mean OH^* signal. With a decrease in flow velocity, the residence time of the species increases, allowing more time for diffusion to occur despite the reduction in length scale of the molecular mean free path. Reduced oxidant availability at 3% coflow O_2 (relative to 6% and 9%) also contributes to the capacity for greater H_2 diffusion across the flame. Assuming that entrainment in a reacting jet follows similar trends as a non-reacting jet, the
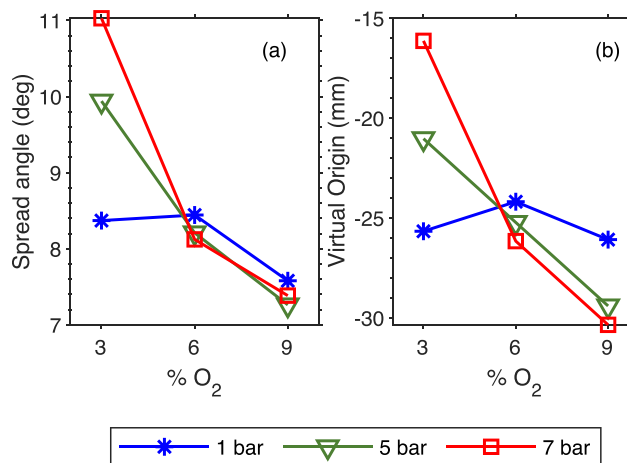

Fig. 4 – (a) OH^* spread angle (b) OH^* concentration virtual origin.

elevated pressure should not have an impact, as the momentum ratio is constant [68]. However, turbulent transport will reduce, as the eddy scales will be smaller. The result is that molecular diffusion of H_2 becomes more dominant as pressure increases. When there is 3% coflow O_2, the flame is weaker as compared to 6% and 9%, and the peak temperatures are lower, resulting in a comparatively low thermal gradient, and lower reactant energy. As a result of the lower thermal gradient and more dominant diffusion, some H_2 is able to pass through the flame more readily, pushing the stoichiometric mixture fraction away from the jet centreline, and hence the OH^* peak value, as noted previously [9,69]. The shift in mixture fraction, and the increased presence of H_2 are discussed further in Section Production of OH^*. Similar observations have been noted at 3% coflow O_2 in atmospheric jets, where it has been shown that the most reactive mixture fraction, as well as the stoichiometric mixture fraction, lie far into the lean side of the flame, rather than within the jet-coflow shear layer [70]. The increased spread in the flame is also contributed to through the increased impact of turbulence interactions with the jet as pressure is increased. From laminar flame calculations discussed in Section Profiles in Mixture Fraction Space, the OH^* mixture fraction width decreases with an increase in pressure, opposing the spatial shift observations here, and hence indicating that turbulence plays a large role in the change in spread angle in addition to the diffusion effects.

The downstream shift in virtual origin for 3% coflow O_2 observed in Fig. 4(b) results in part from the higher diffusivity and low thermal gradient. Due to the high jet-coflow momentum ratio ($\rho_{jet}\overline{U}_{jet}^2 / \rho_{coflow}\overline{U}_{coflow}^2$), ignition is slightly delayed from the development of a fluidic bluff body before mixing becomes dominant, leading to a flame that appears to be lifted several millimeters above the jet exit. Coupling the apparent lift off with the higher spread angle leads to the elevated virtual origin of the OH^* signal.

As the coflow O_2 level increases, the effect of pressure shows differing effects on the virtual origin and spread angle of the peak OH^* signal. At 6% coflow O_2, both virtual origin and spread angle appear to be minimally affected when the pressure is increased. The lack of variation with an increase in pressure suggests that while turbulent transport reduces in intensity, and residence time increases, the higher temperature of combustion minimises the molecular diffusion of H_2. The 6% O_2 flames share similar characteristics across the different pressures. Increasing the coflow O_2 concentration to 9%, the spread angle remains constant, however, the virtual origin is pushed upstream. As will be discussed further in Section H_2 Laminar Flame Characteristics, an increase in coflow O_2 results in higher combustion temperatures from the jet. With the higher jet combustion temperatures in the 6% and 9% coflow O_2 cases relative to the 3% coflow O_2 cases, the larger scale jet motion is restricted, as the lower density products are convected towards the jet centre to conserve mass. As a result of the greater convection, the lower O_2, higher pressure cases are observed to have the greatest OH^* spread. The increased combustion temperature likely contributes to a reduction in diffusion of H_2 across the flame due to the increased reactant energy. These factors contribute to a

narrowing of the overall jet, reducing spread angle slightly, and pushing the virtual origin downstream.

Axial OH^* profiles

In the case of time-averaged OH^* chemiluminescence, which is correlated to the heat release rate, it is useful to determine the "intensity" of the flame by integrating the OH^* signal across radial slices. This gives a measure of the overall OH^* chemiluminescence between the jet centreline, and the flame edge. In addition to the flame intensity, the width of this zone is insightful to the distribution of reactants, and the impact that both coflow O_2 concentration, and pressure, have on the flame. The full-width at half maximum (FWHM) in this context, is a measure of the mean flame width, as determined by the time-averaged presence of OH^*. As such, it includes the time-averaged effects of turbulence on the transport of OH^*. On either side of the peak OH^* signal, such as those shown in Fig. 1(b), there is a location that is half of this signal strength. The FWHM is the distance between these two points. Fig. 5 presents both the integrated intensity (a–c), and the FWHM (d–f) for each axial location of the experimental cases, with ±10% uncertainty of the FWHM.

Fig. 5(a) indicates that overall OH^* intensity decreases as pressure increases, however, at elevated pressure there is a
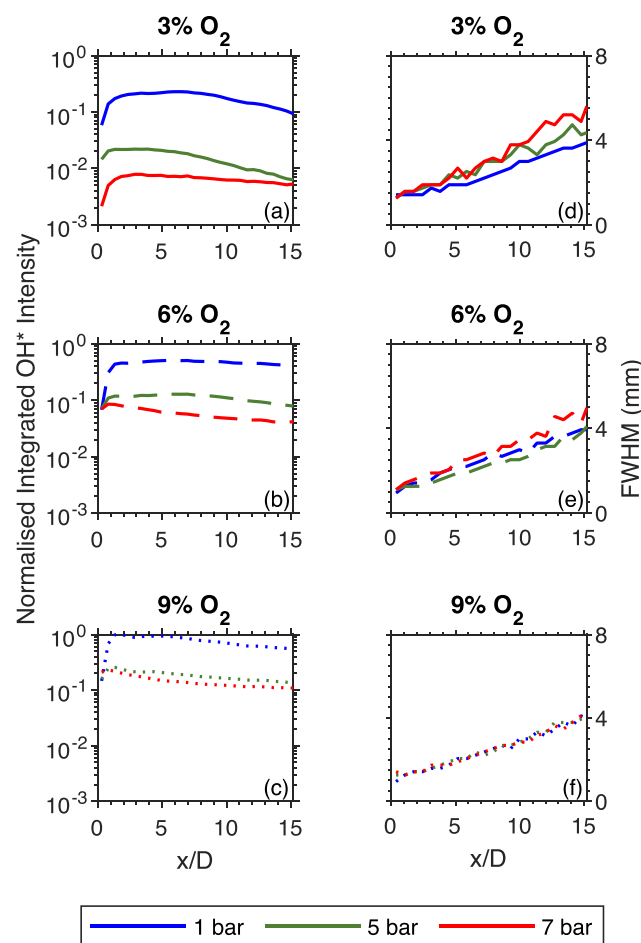

Fig. 5 − (a−c) Axial profiles of integrated OH^* intensity, normalised by peak value across the cases. (d−f) Full-width at half-maximum of OH^* for all cases.

more consistent profile downstream. At 3% coflow O_2 concentration (Fig. 5(d)), there is a noticeable increase in the FWHM as pressure is increased, especially far downstream of the jet exit. So, not only does the OH^* spread increase with pressure (refer Fig. 4(a)), but the flame width increases whilst maintaining overall apparent flame intensity. Additionally, there is a decrease in the OH^* intensity with an increase in pressure, both experimentally, and in laminar flame calculations (refer Section Production of OH^*). Combining the three features of intensity, spread, and FWHM, indicates that increasing pressure at low O_2 results in a transition towards a broader flame. At 6% coflow O_2, there is similar transitional behaviour that can be observed as pressure is increased, however, the increase in FWHM is less prominent, as is the decrease in OH^* intensity. Contrasting the 3% O_2 cases in Fig. 5(a), the most uniform intensity profile is at 1 bar of pressure in Fig. 5(b), although all three pressures show little variation downstream. Comparatively, at 9% coflow O_2 (Fig. 5(f)), there is minimal effect of pressure on the flame width. There is, however, a significant reduction in the OH^* intensity in Fig. 5(c), as in the 6% and 3% O_2 cases. This reduction, along with the consistent FWHM with increased pressure, suggests that while the flame appears to weaken as pressure increases for a coflow O_2 of 9%, it is strong enough to prevent the levels of H_2 diffusion suggested by the 3% O_2 cases.

Laminar flame calculations

Profiles in mixture fraction space

The results of laminar flame calculations, while not directly applicable to the images captured of the CP-JHC flames, can give insight into the chemistry and structure of the flame [10,23,61,71]. Turbulent nonpremixed flames — such as those in this study — can be represented as a continuum of laminar nonpremixed flamelets along the flame sheet, being transported by turbulent fluid motion, and as such, a combination of experimental approaches and laminar flame calculations is often employed to better understand turbulent flame structure [2,9,50,61]. The use of opposed flow laminar flame calculations in this work can provide insight into the behaviour of the flames observed experimentally through the OH^* chemiluminescence. Parameters such as species mole fractions, temperature, and heat release rates can be extracted from flame calculations. Laminar opposed-flow diffusion flame calculations at evaluated pressures from 1 bar to 13 bar, 3–9% O_2 content in the oxidiser, and varying global strain rate ($1 \ s^{-1}$ to $1000 \ s^{-1}$). The concentration of OH and OH^*, along with the net heat of reaction and the temperature are presented in Fig. 6 for several pressures. The strain rate in the chemical simulations presented in Fig. 6 varies such that the inlet velocities decrease with increased pressure, as the mass flow rate remains constant (refer Section Chemical Simulations). However, the influence of changing strain rate or pressure individually, while not directly relevant to the experimental cases that the simulations herein emulate, is still an important factor in characterising the flame behaviour. These trends are discussed further in Section H_2 Laminar Flame Characteristics by looking at the peak values of some variables across the 7500 cases analysed. However, as this does not necessarily demonstrate the mixture fraction based phenomenology of the flame subjected to only a change in pressure, or only a change in strain, a similar analysis as to that which accompanies Fig. 6 can be found in Supplementary Material Section 3 for the constant strain conditions.

Fig. 6 indicates there is correlation in the mixture fraction location corresponding to the peak of the heat release rate and the peak concentration of both OH and OH^*. Across all cases, the mixture fraction location of the peak heat release rate is within ±3.6% of the OH peak, whereas it is within ±9.4% of the OH^* peak. Similar observations have been made with both premixed and non-premixed laminar flame calculations for CH_4-air flames [72,73]. While the correlation in the location of the peak OH^* and peak heat release rate appears to decrease with increased O_2, it is proportional to the width of the reaction zone in mixture fraction space. However, there is still some variation in the correlation. In particular, there is a shift in the peak OH^* number density from the rich to lean side of the reaction zone, while the location of the heat release rate peak remains lean for all cases. Two reasons may contribute to the shift in OH^* peak from the rich to lean flame zone. Firstly, the reactions that contribute most greatly to heat release in the higher oxidant cases involve the reactants that contribute significantly to the quenching of OH^*, most prominently, O_2, H_2, and CO. As such, their participation in the dominant heat release reactions both increases heat release rate at this mixture fraction, and decreases quenching of OH*, resulting in the lean-ward shift in peak OH^* as O_2 increases. Secondly, in the higher O_2 cases, the higher combustion temperatures promote the dissociation of H_2 into H, which diffuses across the stoichiometric mixture fraction, reacting with O_2 to form O and OH (refer Section Production of OH^*). This both increases the number density of OH and presents additional atomic oxygen on the fuel-lean side of the flame to react with atomic hydrogen to form OH^*. This shifts the production of OH^* in favour of the fuel-lean flame, where H, OH, and O radicals are present from the coflow as well. Production of OH^* and the associated trends are explored further in Section Production of OH^*.

Peak OH^* number density (Fig. 6(a), (e), and 6(i)) is close to the stoichiometric mixture fraction (±1.8%), which could be used to help infer the locations of stoichiometric mixture fraction from OH^* chemiluminescence in experiments. In comparison, peak temperature does not correlate strongly with fluorescent species, nor with OH number density, making it difficult to infer further information from the experimental results. Beyond the shift in stoichiometric mixture fraction, there is little change in the morphology of the flame when O_2 content of the oxidiser is increased. As O_2 content is elevated, the temperature rise increases, as oxidant availability rises, and the range of mixture fractions where there is heat release increases. However, at higher pressures, the peak temperature displays an asymptotic approach to a limiting temperature.

The peak OH^* number density at 1 bar in Fig. 6(a), (e), and 6(f), appears to show an increase in value with increased coflow O_2 content, however, it decreases significantly with increased pressure. This trend is noted in experiments as well, with the relative chemiluminescence intensity decreasing tenfold as pressure is increased (refer Fig. 2). At both 6% and
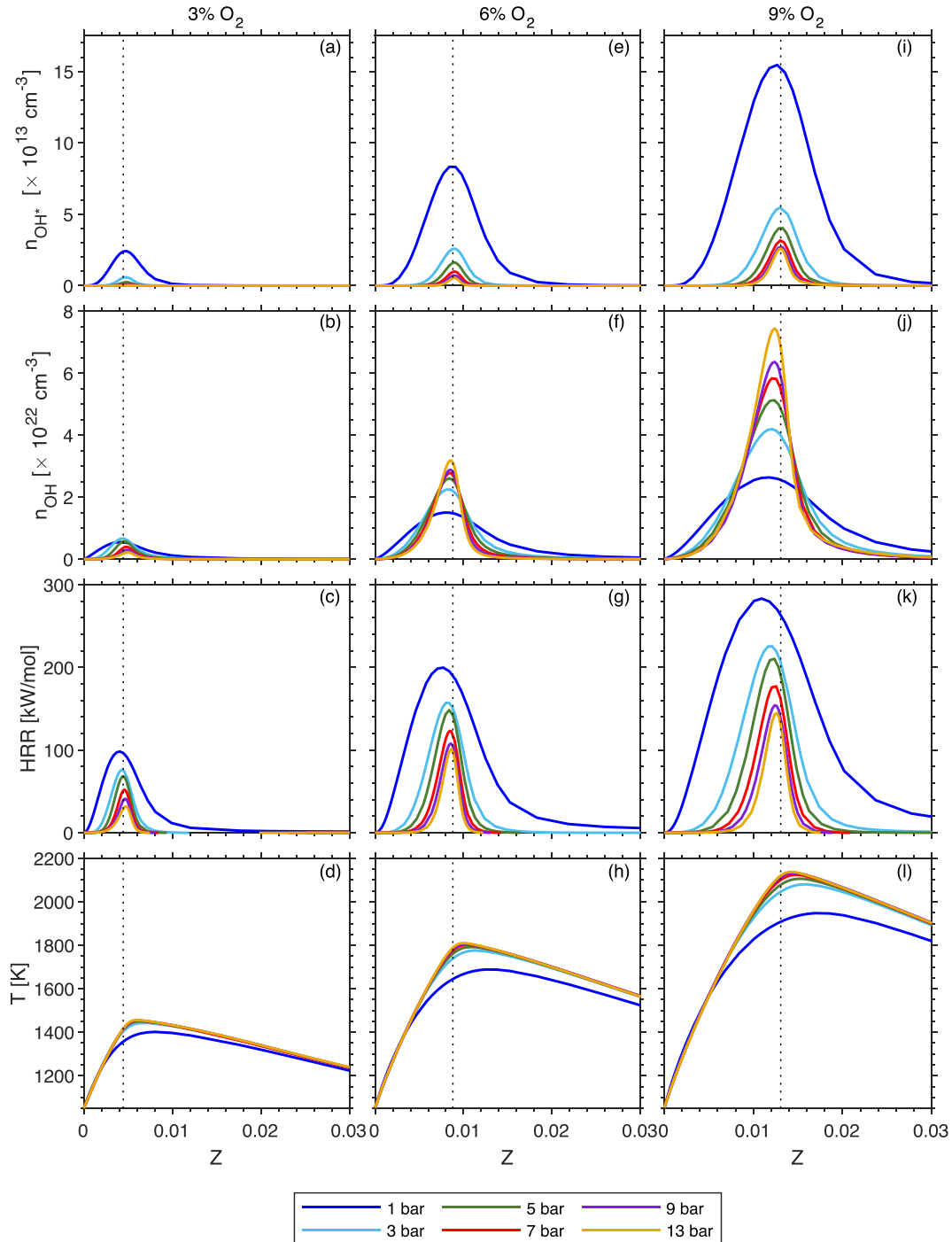
Fig. 6 – **Calculated species number densities, temperatures, and net heat release profiles for different pressures and oxidant levels. (a–d) 3% O$_2$ cases; (e–h) 6% O$_2$ cases; (i–l) 9% O$_2$ cases. Dotted lines indicate stoichiometric mixture fractions.**

9% oxidiser O$_2$, it is interesting to note that while OH* number density decreases with pressure, OH number density, heat release and temperature all rise. However, at 3% O$_2$, the OH number density shows non-monotonic peak behaviour with increased pressure. These phenomena are explored further in Section Production of OH*.
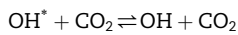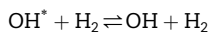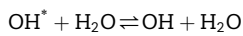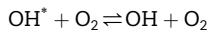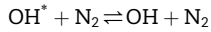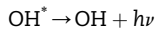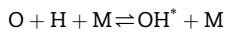
It is also of note that the domain volume based heat release rate shows different trends to the molar based heat release

rate presented here, the differences for which are discussed in the Supplementary Material Section 4.

Production of OH*

To better understand the observations of trends in OH* number density, as well as its relationship to the stoichiometric mixture fraction and maximum heat release discussed in Section Profiles in Mixture Fraction Space, the production of

OH* was analysed. In the kinetic mechanism implemented, ten reactions involving OH* are present:

$$O + H + M \rightleftharpoons OH^* + M \tag{R1}$$

$$OH^* \rightarrow OH + h\nu \tag{R2}$$

$$OH^* + N_2 \rightleftharpoons OH + N_2 \tag{R3}$$

$$OH^* + O_2 \rightleftharpoons OH + O_2 \tag{R4}$$

$$OH^* + H_2O \rightleftharpoons OH + H_2O \tag{R5}$$

$$OH^* + H_2 \rightleftharpoons OH + H_2 \tag{R6}$$

$$OH^* + CO_2 \rightleftharpoons OH + CO_2 \tag{R7}$$

$$OH^* + CO \rightleftharpoons OH + CO \tag{R8}$$

$$CH + O_2 \rightleftharpoons OH^* + CO \tag{R9}$$

$$OH^* + CH_4 \rightleftharpoons OH + CH_4 \tag{R10}$$
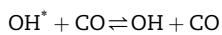
where h is Planck's constant, and ν is the photon frequency of emitted light. With no hydrocarbon fuel in these flames, the presence of CH and CH_4 is negligible aside from the small carbon flux from the fuel mixture in the coflow. In previous investigations, it was found that production of OH* shifts between R1 and R9 with change in oxidant [60], however, this involved using methane as the fuel. With hydrocarbon/hydrogen fuels, the production pathways of OH* are likely to be impacted significantly as the radical pool contains a larger proportion of CH, but changing the oxidiser appears to have limited effect in a pure H_2 flame. As a result, R9 and R10 are neglected throughout this discussion.

The rates of production from reactions R1 through R8, as well as the net rate of these reactions are shown for 3−9% at 1 bar, 9 bar and 13 bar in Fig. 7. The cases shown are at a
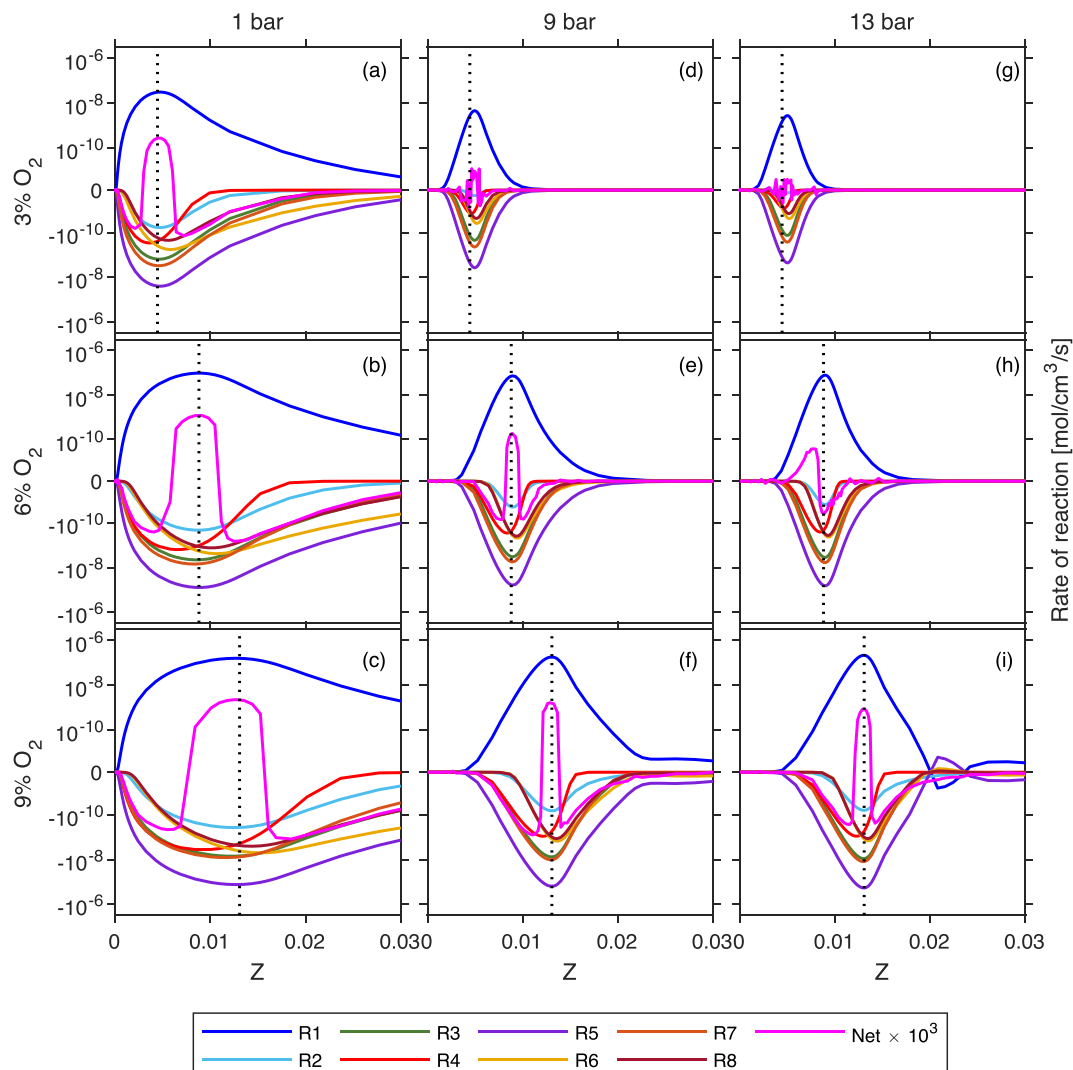

Fig. 7 − Calculated rate of production of OH* from eight key reactions at different O_2 and pressures, as well as the net of these reactions. Dotted line indicates stoichiometric mixture fraction.

constant mass flow rate, as with the experimental work. As such, the strain rate varies with pressure to meet this condition, resulting in lower strain at elevated pressure. All reactions show an increase in magnitude with increased oxidant content, although at varying rates. In particular, both R3 and R7 have marginal changes in magnitude compared with the other reactions, regardless of changes in O_2 content and pressure. These minimal changes are to be expected, given that both N_2, and CO_2 are present in similar quantities across all of the assessed cases.

An increase in pressure decreases the mixture fraction ranges where OH^* reaction rates are elevated. As a result, overall production of OH^* and subsequently the emission of OH^* chemiluminescence is decreased, a trend that is in agreement with the experimental observations (refer Fig. 2). There is a decrease in the overall production of OH^* when pressure is increased, across all O_2 conditions, while an increase in O_2 results in a significant increase in OH^* production. With an increase in pressure, the mixture fraction range for OH^* production narrows significantly around the

stoichiometric mixture fraction. A contributing factor to this reduction is the greater effective contribution of the quenching reactions of R3, R5, and R7 as opposed to the R1 away from the stoichiometric mixture fraction, resulting in a narrowed net production. However, the overall range for R1-R8 decreases with an increase in pressure, a trend that is also noted in Fig. 6 for heat release rate and OH number density. The range reduction results from a shift in the reaction rates of intermediates such as OH, O, and H to form H_2O and HO_2, rather than OH and OH^*, as indicated in Fig. 8. In particular, the production of OH* decreases in magnitude through $O + H + M \rightleftharpoons OH^* + M$, while H_2O and HO_2 production increase significantly through $OH + H_2 \rightleftharpoons H + H_2O$ and $H + O_2 + H_2O \rightleftharpoons HO_2 + H_2O$, especially when the oxidiser O_2 is below 6%.

The 3% O_2 and 9% O_2 show opposing trends for both R1 and R5 as pressure is increased in Fig. 7. At 3% oxidiser O_2, both R1 and R5 decrease in magnitude with increased pressure, however, this trend reverses at 9% oxidiser O_2. R1 is dependent on the presence of atomic O and H, whereas R5 is dependent on the presence of H_2O. However, most of the production of H_2O
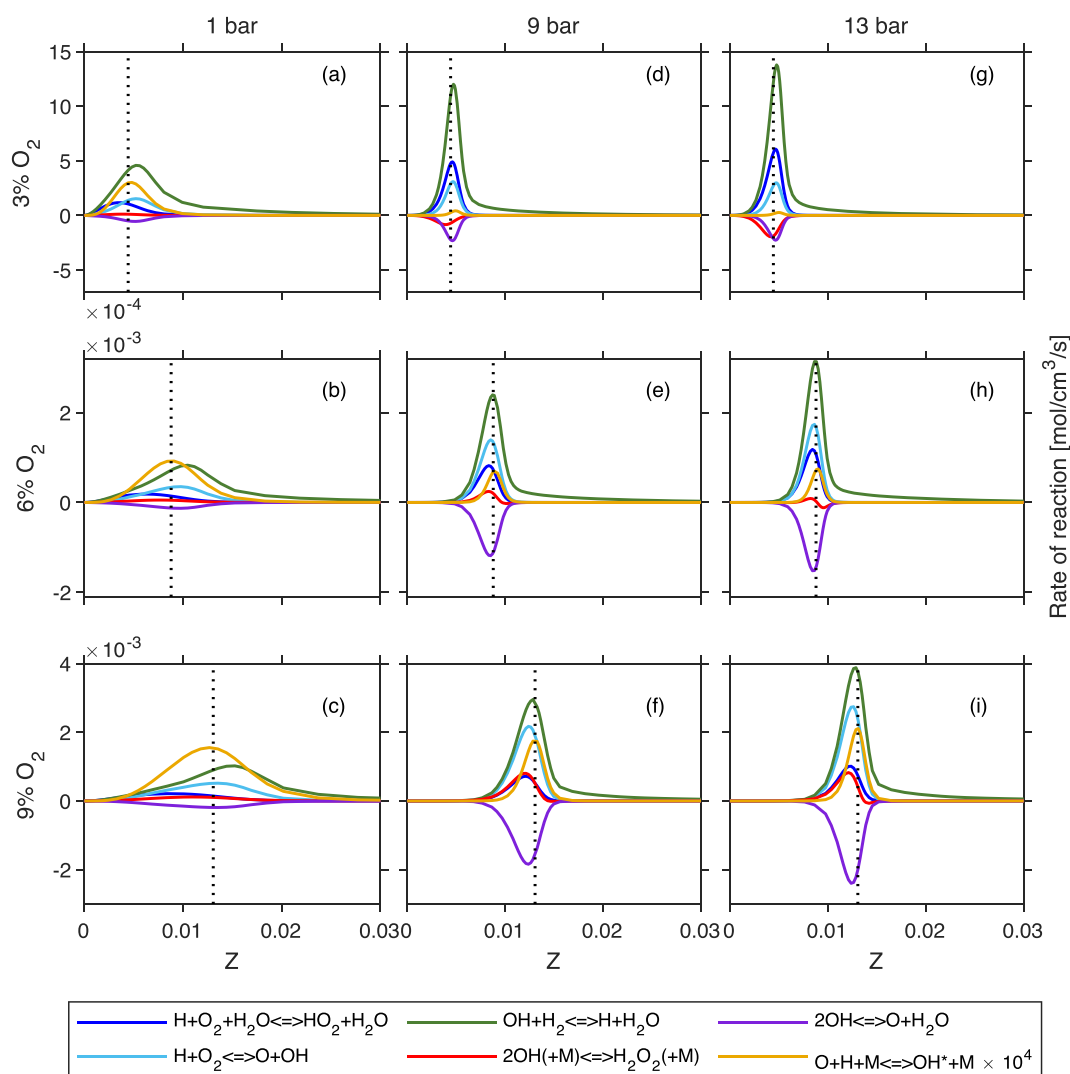

Fig. 8 – Rates of reaction involving H, O, OH, H_2O, and HO_2 that are significantly affected by an increase in pressure. The forward reaction is considered positive here. The dotted black lines indicate the stoichiometric mixture fraction.
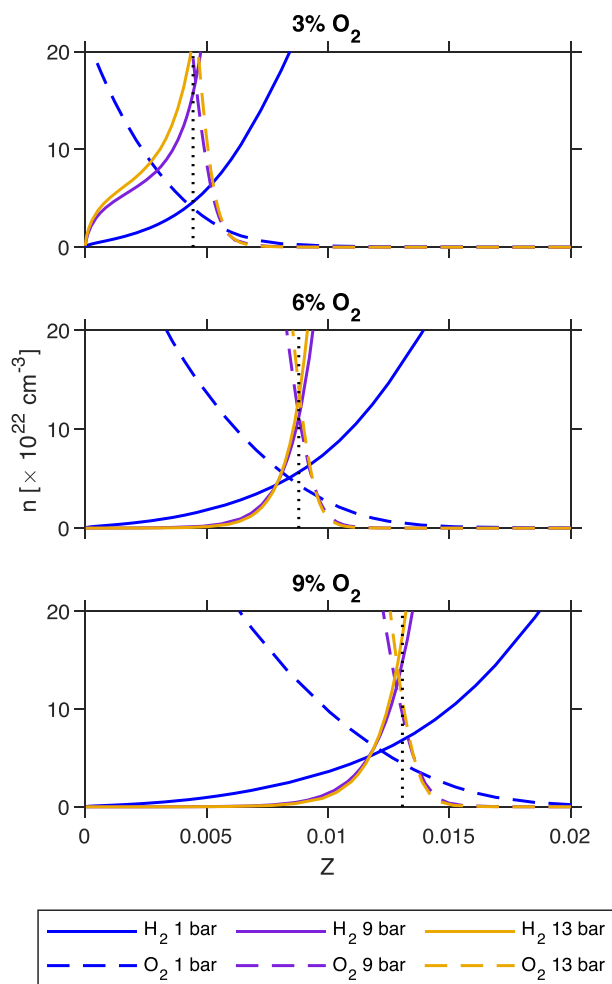
Fig. 9 – Calculated number densities of H_2 and O_2 at select pressures and oxygen concentrations. Dotted lines indicate stoichiometric mixture fraction.

Fig. 10 – Emission of light and production of OH via R2, OH* → OH + $h\nu$, at different O_2 and pressures. Dotted lines indicate stoichiometric mixture fraction.

comes from combination of O and H to form OH, and a subsequent combination of H_2 and OH to form H_2O. The atomic H tends to originate from a decomposition of H_2. Hence, in the lean flame zone, there is a dependence on the presence of H_2 for OH* production, as opposed to O_2 in the rich zone. As such, there is an intrinsic relationship between R1 and R5 through the presence of O_2 and H_2 across the flame. With decreased O_2 content, the lower temperatures may contribute towards the lack of production of atomic O, and hence reduces the overall rate of production of OH* through R1 and R5.

Fig. 9 shows the number density of both H_2 and O_2 as pressure increases for all O_2 levels around the stoichiometric mixture fraction. At 6% and 9% oxidiser O_2, number density of H_2 at elevated pressure is slightly higher than at atmospheric pressure condition, owing to the higher residence time allowing H_2 to diffuse. However, away from the stoichiometric mixture fraction towards the lean side, there is a significant reduction in number density of H_2 at elevated pressure when compared to atmospheric pressure, pointing towards the lean flame edge. Comparatively, in the 3% oxidiser O_2 cases, an increase in pressure results in an overall increase in H_2 number density across the lean flame zone relative to the atmospheric case. The characteristics of the number density
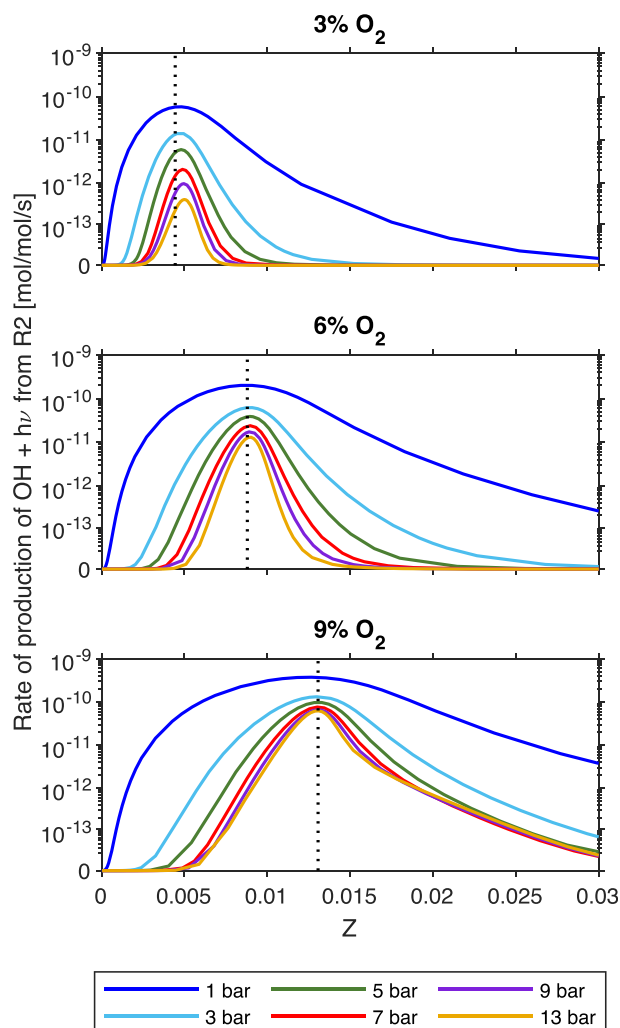
of O_2 in the rich flame zone are similar across the different oxidiser O_2 conditions. An increase in pressure results in an initial increase in number density on the rich side of the stoichiometric mixture fraction, before a more sudden decrease away from this mixture fraction. For 3% O_2, an increase in pressure increases the diffusion of O_2 across the reaction zone, leading to a wider region of potential OH* production. The lower temperature and higher residence time of the elevated pressure 3% O_2 cases allows the H_2 to diffuse across the reaction zone, rather than dissociate into H. The combination of these two diffusion processes may be the cause of the wider OH* spread observed in Figs. 2, 3 and 5, when pressure is elevated at 3% coflow O_2.

Fig. 10 shows the rate of production of OH + $h\nu$ via R2, the chemiluminescence reaction, at pressures from 1 bar to 13 bar and 3–9% O_2. As pressure is increased, a non-linear reduction in the peak OH rate of production is observed at all O_2 levels. As O_2 content is increased, the increase in pressure appears to have a reduced effect on the emission of light from OH*. This correlates with what was observed in Fig. 2, whereby the intensity of OH* signal at 9% O_2 varies little between cases

H9–P5 and H9–P7, as opposed to the variation in 3% O_2 cases, H3–P5 to H3–P7. This asymptotic behaviour is likely due to the limited production of atomic O in the fuel rich environment as O_2 becomes more limited, governing the OH^* availability. The intensity of OH* chemiluminescence in case H3–P7 compared with H9–P1 (refer Fig. 2), is close to two orders of magnitude, which is also represented in Fig. 10. Interestingly, the range of mixture fraction where OH^* is emitted tends to reduce with increased pressure, contrary to the physical space expansion discussed in Section Axial OH^*

Profiles, and to the presence of both H_2 and O_2 presented in Fig. 9. Also notable is the fact that increased pressure tends to shift the location of the peak OH^* chemiluminescence towards the rich side of the flame. This observation is also in direct contrast to the experimental observations (refer Section Typical Appearance). However, the influence of turbulence is not captured in the laminar flame calculations. Fig. 2 is a time-averaged view of a turbulent flame, averaging out any turbulent fluctuations, including turbulent transport of the flamelets. As such, turbulent transport of the mixture fraction range
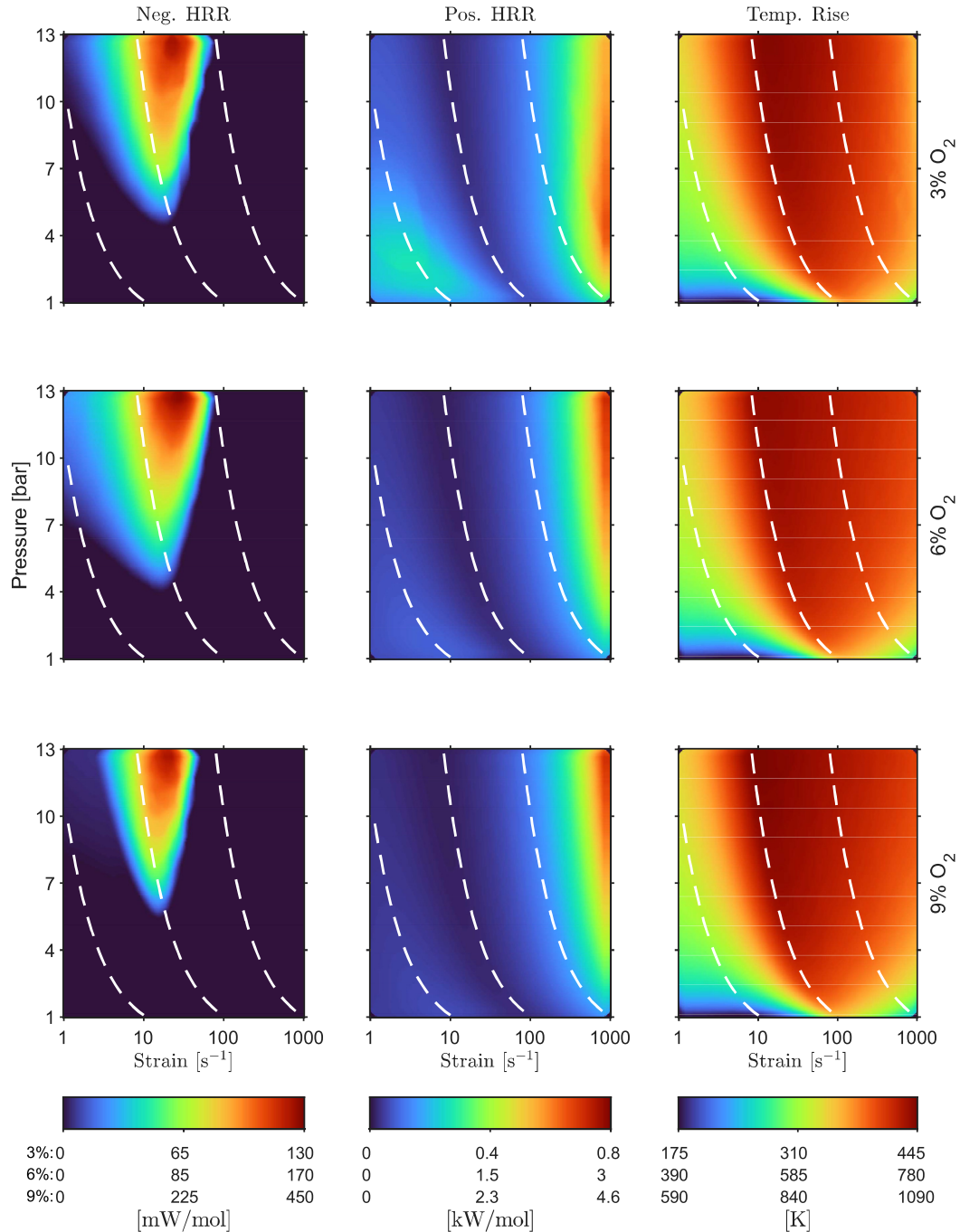

Fig. 11 – **Maximum magnitude of net negative heat release rate, net positive heat release rate, and temperature rise. White dashed lines indicate lines of constant mass flow rate.**

where OH* chemiluminescence occurs may contribute towards the experimental observations after averaging.

H_2 laminar flame characteristics
By simulating a range of non-premixed opposed flow laminar flames, trends in the peak values of low O_2 combustion with pressure can be inferred. Fig. 11 shows the peak magnitude of net negative heat release rate with pressure and strain rate,

alongside the peak positive net heat release rate, and peak temperature rise. In the figures presented in this section, isolines of constant mass flow rate are superimposed onto the regime diagrams. These isolines represent the equivalent strains required to achieve a constant mass flow rate as the atmospheric cases, scaling with pressure. As mentioned in Section Profiles in Mixture Fraction Space, the peak values can be used to infer characteristics of the flames by looking at the
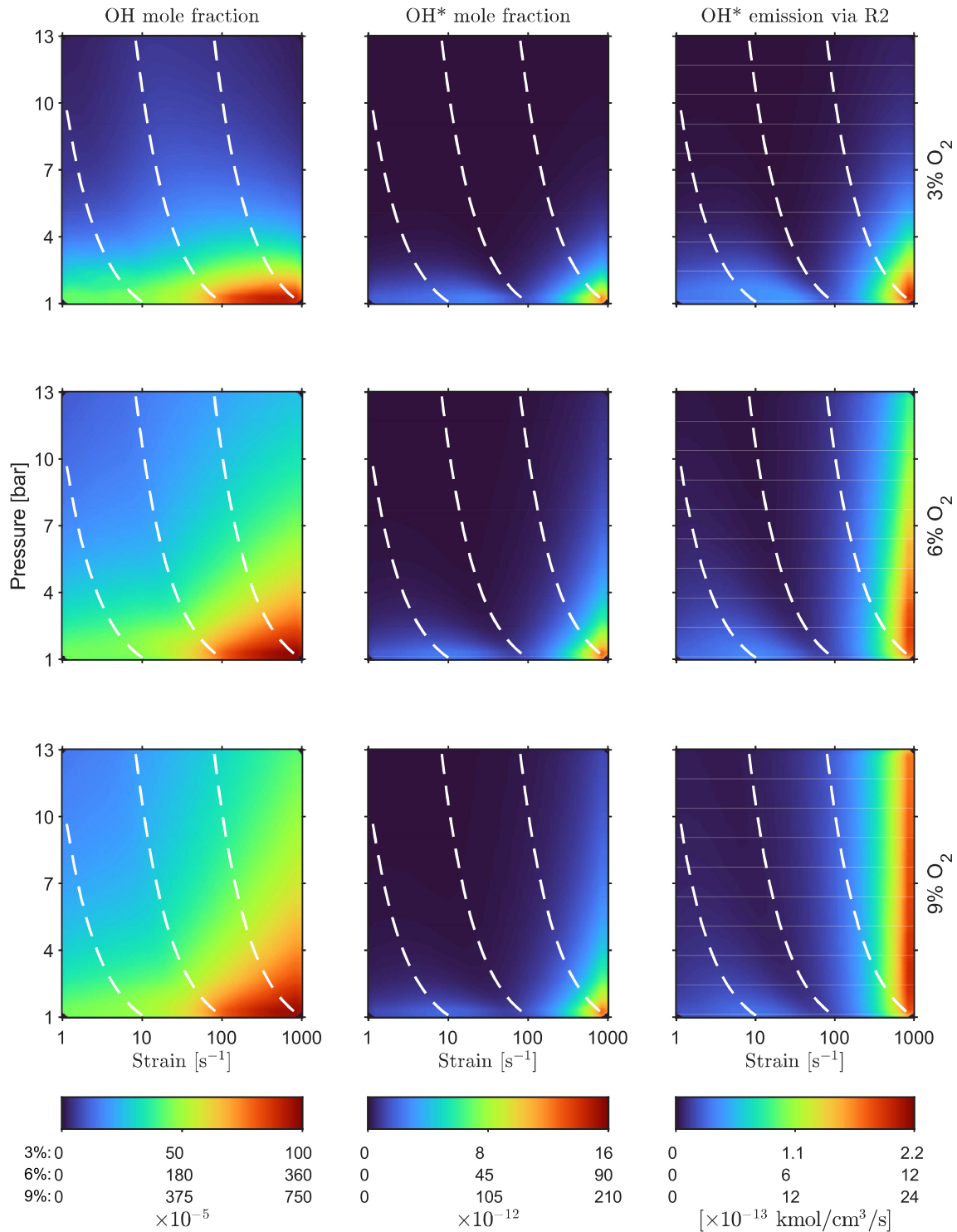

Fig. 12 − Peak mole fractions of OH and OH*, as well as peak rate of reaction from R2, OH* → OH + hν. White dashed lines indicate lines of constant mass flow rate.

trends in Figs. 11 and 12 only vertically (for constant strain and varying pressure), or only horizontally (constant pressure and varying strain), rather than just the isolines presented in white. It is interesting to note that an increase in pressure shows a reversal in trend for the magnitude of the negative heat release, as opposed to the positive heat release.

The absence of a net negative heat release zone is indicative of MILD combustion [8,58]. Fig. 11 indicates that elevating pressure does tend to increase the magnitude of the negative zone. Contrary to observations using hydrocarbon fuels, increasing O_2 in a pure H_2 fuel mixture appears to increase the range of negative heat release cases, rather than decrease them, indicating that MILD combustion is unlikely to be achieved at O_2 levels above 6% for H_2 flames, nor at higher pressures, at least at lower strain rates [58]. However, with increased strain rate, the negative heat release zones disappear. This transition is likely due to the reduced fluid timescale favouring faster oxidation reaction pathways, and hence a net exothermic reaction occurs.

At elevated pressure and lower strain, inhibition of the oxidation reactions tends to occur, especially above the third explosion limit for H_2-O_2 combustion, where chain-branching of $H-O_2$ shifts towards $HO_2-H_2O_2$ branching [38]. The increased residence time pushes the decomposition reactions to dominate, resulting in the trend observed in Fig. 11, whereby lower strain and elevated pressure cases show increased magnitude of net negative heat release rate. In the case of the positive heat release rate in Fig. 11, trends are similar across the different oxidant levels. In the constant mass flow scenario there is a slight increase in peak heat release as pressure rises, but overall minimal variation. However, for a given pressure, the net heat release rate shows non-monotonic variation when strain is increased, with a minimum along the constant mass flow line with a global strain of 100 s^{-1} at 1 bar. This trend represents a larger scale of what is observed in Fig. 6, and in Fig. 10.

Although maximum heat release rate peaks at elevated strain and pressure, the peak temperature rise shown in Fig. 11 follows a line of constant mass flow rate. The temperature rise is lower at elevated strain and low pressure, in line with conventional combustion observations. Trends are consistent across O_2 percentage, however, the range of temperature values varies significantly. Peak temperature rise is aligned with the cases of minimum heat release rate, which is also in agreement with conventional laminar flame characteristics [74,75]. However, there is little other correlation between the heat release rate and the peak temperature rise across the rest of the regime map in Fig. 11, making inference of temperature information from the heat release rate or the OH* chemiluminescence difficult. Peak mole fractions of OH, and OH*, alongside the peak rate of reaction of R2 (refer Section Production of OH*) are shown in Fig. 12 across the cases simulated, alongside the change in temperature relative to the oxidiser.

While an increase in pressure at the same strain tends to result in a monotonic decrease in both OH* mole fraction and OH* chemiluminescence, changes in strain at constant pressure shows non-monotonic variation of both variables. As seen in the 3% O_2 cases, increased pressure at high strain results in an overall reduction of OH mole fraction, likely due to

the increased number density resulting in a greater number of recombination reactions. There is, however, a significant increase in the intensity of OH* chemiluminescence at high strain rate and pressure at both 6% and 9% oxidiser O_2 that is not reflected in the mole fraction of OH*. This suggests that the influence of pressure at elevated strain inhibits to OH* production, but favours de-energisation of OH* through R2. As chemiluminescence requires no third body, the increased number density of OH* is the likely contributor towards the elevated chemiluminescence in the 6% and 9% oxidiser O_2 cases. An increase in strain at constant pressure for OH* mole fraction and OH* chemiluminescence results in non-monotonic variation, characterised by a trough through the middle of the regime diagram and peaks at the extremes of strain. Often, a reduction in strain tends to increase the overall reaction rates, however, this is not observed in these simulations past 100 s^{-1} equivalent strain (accounting for pressure effects) [76]. An increase in strain instead increases the mole fraction of both OH and OH*, suggesting that the mechanism for production of atomic O and atomic H — the primary reactants that form OH and OH* — changes. At 3% oxidiser O_2, there appears to be a strong inverse correlation between rate of reaction of R2, with the peak temperature rise observed in Fig. 11.

MILD combustion in laminar H_2 flames

Several definitions for MILD combustion have previously been proposed, including the perfectly stirred reactor conditions, as well as the net negative heat release rate conditions [7,9]. Using the PSR calculations to determine autoignition temperatures, locations of potential MILD combustion can be identified from Fig. 11. Fig. 13 shows these conditions.
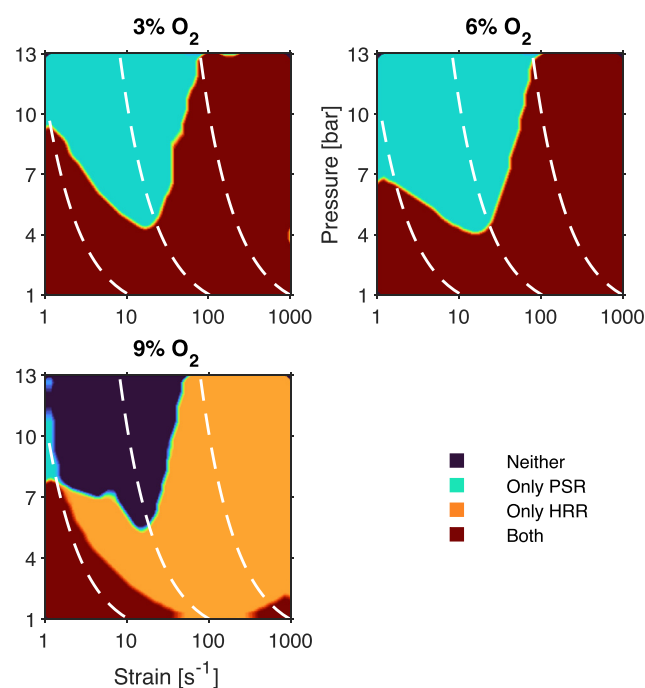

Fig. 13 — MILD combustion based on PSR and negative HRR definitions. White dashed lines are contours of constant mass flow rate.

At low O_2 content (3–6%), capacity for MILD appears to be limited primarily by the net negative heat release, whereas at higher O_2 (9%), the temperature rise is the limiting factor, despite the increase in the magnitude and range of negative heat release zones. As such, there is potential for local zones of MILD combustion to have been observed in the experiments, however, characterisation from OH^* chemiluminescence alone is not feasible, despite the strong correlation between OH^* chemiluminescence and heat release rate discussed in Section Profiles in Mixture Fraction Space and Section H_2 Laminar Flame Characteristics. In particular, at 3–6% O_2, a range of strains and pressures show the potential for MILD combustion to occur, with some possibility in the low pressure range for 9%. Given the low strain rates however, it is unlikely that a realistic turbulent flame will have low enough strain rates at these pressures to accommodate MILD combustion.

Conclusions

Hydrogen jet flames in a hot and vitiated coflow have been characterised at pressures from 1 bar to 7 bar, using a combination of experimental OH^* chemiluminescence imaging and laminar flame calculations. The main findings from this work are summarised as follows:

- The mixture fraction location of peak OH^* number density correlates strongly with that of peak HRR and with the stoichiometric mixture fraction, across the range of pressures from 1 bar to 13 bar, especially when the oxidant has <6% O_2.
- Increases in pressure and reduction in O_2 both decrease OH^* intensity in experimental flames, and in laminar flame calculations, owing primarily to increased collisional quenching of OH^* (relative to production) and preferential formation of OH, HO_2 and H_2O with increased pressure.
- Higher flame temperatures were observed with an increase in pressure in laminar flame calculations, whereas heat release rate (HRR) decreased.
- The mixture fraction range where OH^* is present in laminar flame calculations decreases with increased pressure, opposing the observed physical widening of the OH^* signal in experiments. The difference is attributed to the influence of turbulence in the experiments leading to a smearing in the mean measurement.
- Changes in pressure have a more significant impact on flame characteristics with a 3% O_2 coflow, as compared with 6% or 9%.
- At 3% O_2, increases in pressure increased the full-width at half-maximum (FWHM) of the OH^* profile and the spread angle, and shifted the OH^* virtual origin upstream.
- At 3% O_2, integrated radial OH^* signal remained nearly constant at high pressure, despite increases to FWHM, indicating a shift towards a spatially broadened flame at low O_2 levels.

- Diffusion of H_2 and O_2 across the stoichiometric mixture fraction is more prevalent at 3% O_2 than at 6% or 9% as indicated by laminar flame calculations, contributing towards the wider OH^* FWHM observed in the experiments.
- The perfectly stirred reactor and heat release rate criterion for MILD combustion are met by laminar hydrogen flames across a large range of pressures and strain rates for 3% and 6% oxidiser O_2, but not 9%.

The above findings indicate that as oxygen is reduced in the oxidiser stream of a hydrogen jet flame, changes to the environmental pressure have a more significant effect on the flame characteristics. The result of lowering the oxygen level and increasing pressure is a shift towards MILD combustion conditions, however, further experimental work with more advanced diagnostics would be necessary to better classify these regimes. In summary, this work highlights the potential for MILD combustion of hydrogen in high pressure devices, such as advanced gas turbines.

Declaration of competing interest

The authors declare that they have no known competing financial interests or personal relationships that could have appeared to influence the work reported in this paper.

Acknowledgements

Appendix A. Supplementary data

Supplementary data to this article can be found online at https://doi.org/10.1016/j.ijhydene.2023.02.053.

REFERENCES

[1] Diez LI, Cortés C, Pallarés J. Numerical investigation of NOx emissions from a tangentially-fired utility boiler under conventional and overfire air operation. Fuel 2008;87(7):1259–69.

[2] Dally BB, Karpetis A, Barlow R. Structure of turbulent non-premixed jet flames in a diluted hot coflow. Proc Combust Inst 2002;29(1):1147–54.

[3] Galbiati MA, Cavigiolo A, Effuggi A, Gelosa D, Rota R. Mild combustion for fuel-NOx reduction. Combust Sci Technol 2004;176(7):1035–54.

[4] Li P, Wang F, Mi J, Dally B, Mei Z, Zhang J, Parente A. Mechanisms of NO formation in MILD combustion of CH_4/

H₂ fuel blends. Int J Hydrogen Energy 2014;39(33):19187−203.

[5] Stadler H, Ristic D, Förster M, Schuster A, Kneer R, Scheffknecht G. NOx-emissions from flameless coal combustion in air, Ar/O₂ and CO₂/O₂. Proc Combust Inst 2009;32(2):3131−8.

[6] Shi G, Li P, Hu F, Liu Z. NO mechanisms of syngas MILD combustion diluted with N₂, CO₂, and H₂O. Int J Hydrogen Energy 2022;47(37):16649−64.

[7] Cavaliere A, De Joannon M. Mild combustion. Prog Energy Combust Sci 2004;30(4):329−66.

[8] de Joannon M, Sabia P, Sorrentino G, Cavaliere A. Numerical study of mild combustion in hot diluted diffusion ignition (HDDI) regime. Proc Combust Inst 2009;32(2):3147−54.

[9] Ye J, Medwell PR, Evans MJ, Dally BB. Characteristics of turbulent n-heptane jet flames in a hot and diluted coflow. Combust Flame 2017;183:330−42.

[10] Evans M, Medwell P, Wu H, Stagni A, Ihme M. Classification and lift-off height prediction of non-premixed MILD and autoignitive flames. Proc Combust Inst 2017;36(3):4297−304.

[11] Dally BB, Riesmeier E, Peters N. Effect of fuel mixture on moderate and intense low oxygen dilution combustion. Combust Flame 2004;137(4):418−31.

[12] Medwell PR, Kalt PA, Dally BB. Imaging of diluted turbulent ethylene flames stabilized on a Jet in Hot Coflow (JHC) burner. Combust Flame 2008;152(1−2):100−13.

[13] Evans M, Sidey J, Ye J, Medwell P, Dally B, Mastorakos E. Temperature and reaction zone imaging in turbulent swirling dual-fuel flames. Proc Combust Inst 2019;37(2):2159−66.

[14] Li P, Mi J, Dally B, Wang F, Wang L, Liu Z, Chen S, Zheng C. Progress and recent trend in MILD combustion. Sci China Technol Sci 2011;54(2):255−69.

[15] Bond TC, Streets DG, Yarber KF, Nelson SM, Woo J-H, Klimont Z. A technology-based global inventory of black and organic carbon emissions from combustion. J Geophys Res Atmos 2004;109(D14).

[16] Gao X, Duan F, Lim SC, Yip MS. NOx formation in hydrogen−methane turbulent diffusion flame under the moderate or intense low-oxygen dilution conditions. Energy 2013;59:559−69.

[17] Ferrarotti M, Amaduzzi R, Bascherini D, Galletti C, Parente A. Heat release rate markers for the Adelaide jet in hot coflow flame. Front Mech Eng 2020;6:5.

[18] Mendez LA, Tummers M, Van Veen E, Roekaerts D. Effect of hydrogen addition on the structure of natural-gas jet-in-hot-coflow flames. Proc Combust Inst 2015;35(3):3557−64.

[19] Liu G, Li S. Lift-off height of autoignited jet flame in hot air coflow with different O₂ contents. Combust Flame 2022;242:112144.

[20] Ramachandran A, Narayanaswamy V, Lyons KM. Observations on the role of auto-ignition in flame stabilization in turbulent non-premixed jet flames in vitiated coflow. J Eng Gas Turbines Power 2019;141(6).

[21] Wu Z, Xie W, Zhang E, Yu Y, Qin Q, Deng J, Li L. Investigation of flame characteristics of hydrogen jet issuing into a hot vitiated nitrogen/argon/carbon dioxide coflow. Int J Hydrogen Energy 2019;44(52):28357−70.

[22] Liu Z, Xiong Y, Zhu Z, Zhang Z, Liu Y. Effects of hydrogen addition on combustion characteristics of a methane fueled mild model combustor. Int J Hydrogen Energy 2022;47(36):16309−20.

[23] Cabra R, Myhrvold T, Chen J, Dibble R, Karpetis A, Barlow R. Simultaneous laser Raman-Rayleigh-LIF measurements and numerical modeling results of a lifted turbulent H₂/N₂ jet flame in a vitiated coflow. Proc Combust Inst 2002;29(2):1881−8.

[24] Mardani A, Tabejamaat S. Effect of hydrogen on hydrogen−methane turbulent non-premixed flame under mild condition. Int J Hydrogen Energy 2010;35(20):11324−31.

[25] Ferrarotti M, De Paepe W, Parente A. Reactive structures and nox emissions of methane/hydrogen mixtures in flameless combustion. Int J Hydrogen Energy 2021;46(68):34018−45.

[26] Ye J, Medwell PR, Kleinheinz K, Evans MJ, Dally BB, Pitsch HG. Structural differences of ethanol and DME jet flames in a hot diluted coflow. Combust Flame 2018;192:473−94.

[27] Gopan A, Kumfer BM, Axelbaum RL. Effect of operating pressure and fuel moisture on net plant efficiency of a staged, pressurized oxy-combustion power plant. Int J Greenh Gas Control 2015;39:390−6.

[28] Porpatham E, Ramesh A, Nagalingam B. Effect of compression ratio on the performance and combustion of a biogas fuelled spark ignition engine. Fuel 2012;95:247−56.

[29] Moran MJ, Shapiro HN, Boettner DD, Bailey MB. Fundamentals of engineering thermodynamics. John Wiley & Sons; 2010.

[30] Stöhr M, Arndt CM, Meier W. Effects of Damköhler number on vortex−flame interaction in a gas turbine model combustor. Proc Combust Inst 2013;34(2):3107−15.

[31] Lewandowski MT, Parente A, Pozorski J. Generalised Eddy Dissipation Concept for MILD combustion regime at low local Reynolds and Damköhler numbers. Part 1: model framework development. Fuel 2020;278:117743.

[32] Parente A, Malik MR, Contino F, Cuoci A, Dally BB. Extension of the Eddy Dissipation Concept for turbulence/chemistry interactions to MILD combustion. Fuel 2016;163:98−111.

[33] Evans M, Petre C, Medwell PR, Parente A. Generalisation of the eddy-dissipation concept for jet flames with low turbulence and low Damköhler number. Proc Combust Inst 2019;37(4):4497−505.

[34] Dally B, Fletcher D, Masri A. Flow and mixing fields of turbulent bluff-body jets and flames. Combust Theor Model 1998;2(2):193.

[35] Brodkey R. Turbulence in mixing operations: theory and application to mixing and reaction. Elsevier; 2012.

[36] Kruse S, Kerschgens B, Berger L, Varea E, Pitsch H. Experimental and numerical study of mild combustion for gas turbine applications. Appl Energy 2015;148:456−65.

[37] Benson SW, Berson JA. The effect of pressure on the rate and equilibrium constants of chemical reactions. The calculation of activation volumes by application of the Tait equation. J Am Chem Soc 1962;84(2):152−8.

[38] Law C. Propagation, structure, and limit phenomena of laminar flames at elevated pressures. Combust Sci Technol 2006;178(1−3):335−60.

[39] Kéromnès A, Metcalfe WK, Heufer KA, Donohoe N, Das AK, Sung C-J, Herzler J, Naumann C, Griebel P, Mathieu O, et al. An experimental and detailed chemical kinetic modeling study of hydrogen and syngas mixture oxidation at elevated pressures. Combust Flame 2013;160(6):995−1011.

[40] Severin M, Lammel O, Ax H, Lückerath R, Meier W, Aigner M, Heinze J. High momentum jet flames at elevated pressure: detailed investigation of flame stabilization with simultaneous particle image velocimetry and OH-LIF. J Eng Gas Turbines Power 2017;140(4):11.

[41] Ax H, Lammel O, Lückerath R, Severin M. High-momentum jet flames at elevated pressure, C: statistical distribution of thermochemical states obtained from laser-Raman measurements. J Eng Gas Turbines Power 2020;142(7). 07.

[42] Guiberti TF, Krishna Y, Boyette W, Yang C, Roberts W, Magnotti G. Single-shot imaging of major species and OH mole fractions and temperature in non-premixed H₂/N₂ flames at elevated pressure. Proc Combust Inst 2021;38(1):1647−55.

[43] Mardani A, Tabejamaat S, Ghamari M. Numerical study of influence of molecular diffusion in the mild combustion regime. Combust Theor Model 2010;14(5):747–74.

[44] Göktolga MU, van Oijen JA, de Goey LPH. 3D DNS of MILD combustion: a detailed analysis of heat loss effects, preferential diffusion, and flame formation mechanisms. Fuel 2015;159:784–95.

[45] van Oijen J. Direct numerical simulation of autoigniting mixing layers in mild combustion. Proc Combust Inst 2013;34(1):1163–71.

[46] Rieth M, Gruber A, Williams FA, Chen JH. Enhanced burning rates in hydrogen-enriched turbulent premixed flames by diffusion of molecular and atomic hydrogen. Combust Flame 2022;239:111740.

[47] Almutairi F, Dinesh KR, van Oijen J. Modelling of hydrogen-blended dual-fuel combustion using flamelet-generated manifold and preferential diffusion effects. Int J Hydrogen Energy 2022.

[48] Saini P, Chterev I, Pareja J, Aigner M, Boxx I. Effect of pressure on hydrogen enriched natural gas jet flames in crossflow. Flow, Turbul Combust 2020;105(3):787–806.

[49] Yip HL, Srna A, Wehrfritz A, Kook S, Hawkes ER, Chan QN. A parametric study of autoigniting hydrogen jets under compression-ignition engine conditions. Int J Hydrogen Energy 2022.

[50] Proud DB, Evans MJ, Chan QN, Medwell PR. Characteristics of turbulent flames in a confined and pressurised jet-in-hot-coflow combustor. J Energy Inst 2022.

[51] Panoutsos C, Hardalupas Y, Taylor A. Numerical evaluation of equivalence ratio measurement using OH* and CH* chemiluminescence in premixed and non-premixed methane–air flames. Combust Flame 2009;156(2):273–91.

[52] Hall JM, Petersen EL. An optimized kinetics model for OH chemiluminescence at high temperatures and atmospheric pressures. Int J Chem Kinet 2006;38(12):714–24.

[53] Dribinski V, Ossadtchi A, Mandelshtam VA, Reisler H. Reconstruction of Abel-transformable images: the Gaussian basis-set expansion Abel transform method. Rev Sci Instrum 2002;73(7):2634–42.

[54] Smith GP, Golden DM, Frenklach M, Moriarty NW, Eiteneer B, Goldenberg M, Bowman CT, Hanson RK, Song S, G. Jr WC, Lissianski VV, Qin Z. GRI-Mech 3.0. 2000. http://www.me.berkeley.edu/gri_mech/.

[55] Tamura M, Berg PA, Harrington JE, Luque J, Jeffries JB, Smith GP, Crosley DR. Collisional quenching of CH (A), OH (A), and NO (A) in low pressure hydrocarbon flames. Combust Flame 1998;114(3–4):502–14.

[56] Porter R, Clark A, Kaskan W, Browne W. A study of hydrocarbon flames. Symposium (International) on Combustion 1967;11(1):907–17.

[57] Devriendt K, Van Look H, Ceursters B, Peeters J. Kinetics of formation of chemiluminescent CH ($A^2\Delta$) by the elementary reactions of C_2H ($X^2\Sigma^+$) with O (^3P) and O_2 ($X^3\Sigma_g^-$): a pulse laser photolysis study. Chem Phys Lett 1996;261(4–5):450–6.

[58] Ye J, Medwell PR, Dally BB, Evans MJ. The transition of ethanol flames from conventional to MILD combustion. Combust Flame 2016;171:173–84.

[59] Sidey J, Mastorakos E. Visualisation of turbulent swirling dual-fuel flames. Proc Combust Inst 2017;36(2):1721–7.

[60] He L, Guo Q, Gong Y, Wang F, Yu G. Investigation of OH* chemiluminescence and heat release in laminar methane–oxygen co-flow diffusion flames. Combust Flame 2019;201:12–22.

[61] Medwell PR, Evans MJ, Chan QN, Katta VR. Laminar flame calculations for analyzing trends in autoignitive jet flames in a hot and vitiated coflow. Energy Fuels 2016;30(10):8680–90.

[62] de Joannon M, Sabia P, Tregrossi A, Cavaliere A. Dynamic behavior of methane oxidation in premixed flow reactor. Combust Sci Technol 2004;176(5–6):769–83.

[63] de Joannon M, Cavaliere A, Faravelli T, Ranzi E, Sabia P, Tregrossi A. Analysis of process parameters for steady operations in methane mild combustion technology. Proc Combust Inst 2005;30(2):2605–12.

[64] Sabia P, Sorrentino G, Chinnici A, Cavaliere A, Ragucci R. Dynamic behaviors in methane MILD and oxy-fuel combustion. Chemical effect of CO_2, Energy & Fuels 2015;29(3):1978–86.

[65] Yoo CS, Chen JH, Frank JH. A numerical study of transient ignition and flame characteristics of diluted hydrogen versus heated air in counterflow. Combust Flame 2009;156(1):140–51.

[66] Echekki T, Chen JH. Direct numerical simulation of autoignition in non-homogeneous hydrogen-air mixtures. Combust Flame 2003;134(3):169–91.

[67] Uddin M, Pollard A. Self-similarity of coflowing jets: the virtual origin. Phys Fluids 2007;19(6):068103.

[68] Han D, Mungal M. Direct measurement of entrainment in reacting/nonreacting turbulent jets. Combust Flame 2001;124(3):370–86.

[69] Sidey JA, Allison PM, Mastorakos E. The effect of fuel composition on swirling kerosene flames. 55th AIAA Aerospace Sciences Meeting; 2017. 0383.

[70] Evans M, Chinnici A, Medwell P, Ye J. Ignition features of methane and ethylene fuel-blends in hot and diluted coflows. Fuel 2017;203:279–89.

[71] Sahoo A, Ramachandran A, Narayanaswamy V, Lyons KM. Mixture fraction measurement in turbulent non-premixed MILD jet flame using Rayleigh scattering. Appl Opt 2022;61(9):2338–51.

[72] Fayoux A, Zähringer K, Gicquel O, Rolon J-C. Experimental and numerical determination of heat release in counterflow premixed laminar flames. Proc Combust Inst 2005;30(1):251–7.

[73] Sidey JA, Mastorakos E. Simulations of laminar non-premixed flames of methane with hot combustion products as oxidiser. Combust Flame 2016;163:1–11.

[74] Lyon RE. Heat release kinetics, Fire and Materials 2000;24(4):179–86.

[75] Darabiha N. Transient behaviour of laminar counterflow hydrogen-air diffusion flames with complex chemistry. Combust Sci Technol 1992;86(1–6):163–81.

[76] Darabiha N, Candel S, Marble F. The effect of strain rate on a premixed laminar flame. Combust Flame 1986;64(2):203–17.